



This is the published version of the following conference paper:

Khan, Razmi, Eichmann, Troy, Buttsworth, David, & [Upcroft, Ben](#) (2011) Image-based visual servoing for the super-orbital re-entry of Hayabusa spacecraft. In *Proceedings of 2011 Australasian Conference on Robotics and Automation*, Australian Robotics and Automation Association Inc., Monash University, Melbourne, VIC.

Copyright 2011 Please consult the authors.

# Image-Based Visual Servoing for the Super-Orbital Re-Entry of Hayabusa Spacecraft

Razmi Khan\*

University of Queensland, Brisbane, Queensland, 4072, Australia  
razmi.khan@uqconnect.edu.au

Troy Eichmann†

University of Queensland, Brisbane, Queensland, 4072, Australia  
tneichmann@internode.on.net

David Buttsworth‡

University of Southern Queensland, Toowoomba, Queensland, 4350, Australia  
david.buttsworth@usq.edu.au

Ben Upcroft§

University of Queensland, Brisbane, Queensland, 4072, Australia  
upcroft@gmail.com

## Abstract

This paper presents an image-based visual servoing system that was used to track the atmospheric Earth re-entry of Hayabusa. The primary aim of this ground based tracking platform was to record the emission spectrum radiating from the superheated gas of the shock layer and the surface of the heat shield during re-entry.

To the author's knowledge, this is the first time that a visual servoing system has successfully tracked a super-orbital re-entry of a spacecraft and recorded its spectral signature. Furthermore, we improve the system by including a simplified dynamic model for feed-forward control and demonstrate improved tracking performance on the International Space Station (ISS).

We present comparisons between simulation and experimental results on different target trajectories including tracking results from Hayabusa and ISS. The required performance for tracking both spacecraft is demanding when combined with a narrow field of view (FOV). We also briefly discuss the preliminary results obtained from the spectroscopy of the Hayabusa's heat shield during re-entry.



Fig. 1. PTU and camera equipment used for the Hayabusa re-entry

## 1 Introduction

Hayabusa is an unmanned Japanese spacecraft that was launched as a scientific mission to collect samples from asteroid Itokawa [Uesugi 2003]. Although many difficulties were experienced the ambitious mission achieved many 'firsts' and the capsule successfully re-entered the Earth at super-orbital velocities. These high velocities, in the order of 12km/s provided a rare opportunity to experimentally measure radiation emitted

---

\* Postgraduate Student, School of Mechanical and Mining Engineering

† Postgraduate Student, School of Mathematics and Physics

‡ Professor, Faculty of Engineering and Surveying

§ Senior Lecturer, School of Mechanical and Mining Engineering

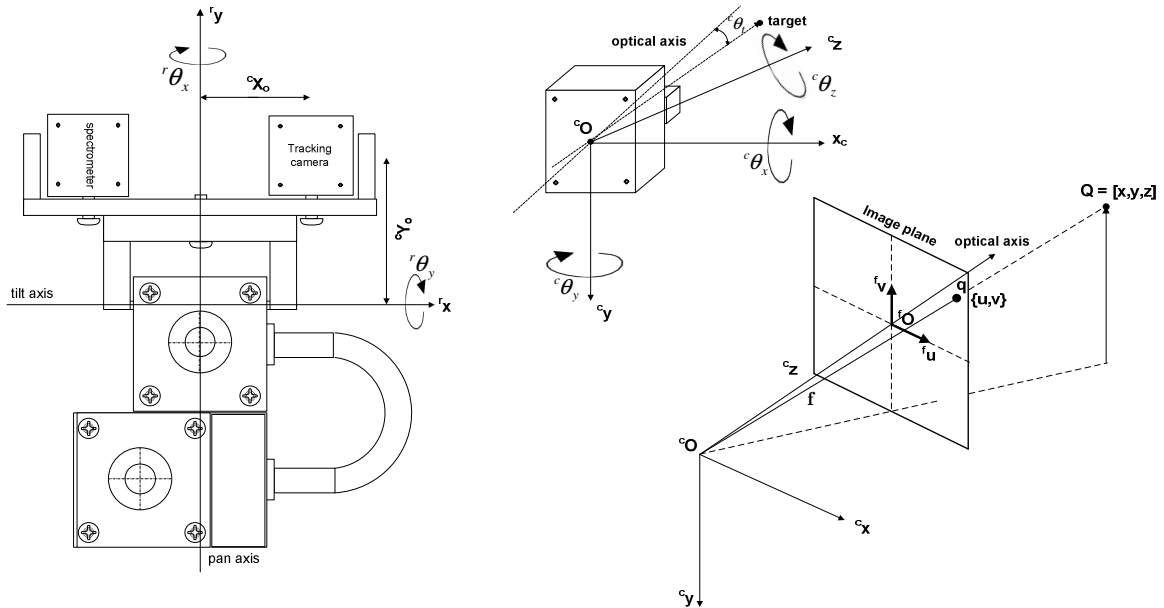


Fig. 2. The PTU (left) is shown with 2-DOF rotational movement and camera mountings. Figures on the right top and bottom demonstrate the camera coordinate system in terms of which, all modelling will be shown and a typical target position on the image plane with an error condition respectively.

from the shock-compressed air in front of the spacecraft and from the capsule heat shield under true flight conditions.

Previous attempts to acquire re-entry radiation signatures on the Stardust [Winter et al., 2007], [McHarg et al., 2008], [Jenniskens, 2008] and Genesis [Jenniskens et al., 2006] spacecraft capsules and the heat distribution on the Space Shuttle [Horvath et al., 2010] were carried out by manually pointing the cameras at the surface of the re-entering vehicle. During such observations, acquiring and tracking the target can be difficult because of human errors. Loss of valuable emissions data for all or part of the re-entry event has occurred on some of these observations due to reliance on manual tracking. To address this problem, we take an automated image-based approach that robustly maintains the alignment of the instruments with the target.

We implemented a visual feedback control strategy, based on concepts described by Papanikolopoulos [Papanikolopoulos et al., 1993] and Hutchinson [Hutchinson et al., 1996] to track the re-entry. The approach required that the target be initially identified manually in an image sequence which is subsequently automatically tracked using a 2 axis pan and tilt unit. The image based tracking is done by implementing Lucas Kanade pyramidal optical flow approach [Bouguet, 1981]. Image intensity contrasts are used to visually track the front edge of the spacecraft's sample return capsule (SRC). This allowed the SRC to be reliably tracked without the possibility of tracking deviations on the plasma emissions tail or the fragments of the main spacecraft\* debris.

To obtain the spectrum of the radiation emitted from the surface of the re-entering vehicle, a spectrometer co-aligned to the tracking camera was implemented. A basic spectrometer was set up which includes a near infra-

red transmission grating attached before the camera lens. The equipment was spatially and spectrally calibrated to record the desired range of wavelengths on the camera CCD.

The tracking of the Hayabusa spacecraft re-entry was automated by utilizing visual feedback control. This method was found to be sufficient to track and obtain spectral information during the re-entry using low magnification wide FOV cameras which provided limited spatial resolution of the SRC. To obtain temperature of the SRC shock layer as a function of surface area, a much higher spatial resolution would be required resulting in the implementation of large focal length lens. This effectively reduces the observed FOV of the cameras and requires much smaller margins of error in tracking the object. To meet this demanding requirement we improve the control by adding a simplified dynamic model of the system.

The model enables feed-forward control which is implemented post re-entry and tested on various target trajectories based on work undertaken by Corke et al. [Corke et al., 1996]. This control strategy is one of only a small number of applications in which feed-forward is implemented. Song [Song et al., 2009] demonstrates feed-forward compensation for high performance tracking on a six DOF robotic arm. Bernardino [Bernardino et al., 1999] demonstrates a binocular visual servoing framework that uses both kinematic and dynamic control strategies for high performance tracking of objects.

We undertake an additional field experiment which involved the tracking of the ISS post the Hayabusa re-entry to show the improvements in the tracking performance using feed-forward as compared to feedback alone. The use of a narrow FOV camera lens resulted in a challenging target trajectory across the image plane with a relative observed velocity between the optics and the ISS similar to a super-orbital re-entry observation. The results from both visual kinematic and dynamic control strategies are discussed.

\* Spacecraft or main spacecraft here refers to the space probe following separation of the SRC

The layout of the paper is as follows; a brief outline of the equipment setup and formation of an Image Jacobian will be discussed in Section 2. In Sections 3 and 4 we model the feedback and feedforward control strategies and present the tracking performance results for different target trajectories. Section 5 details the experiments conducted in simulation and with the actual system. Section 6 describes the visual tracking performance and emission spectra acquired during the Hayabusa spacecraft re-entry. The paper concludes with a discussion on the use of automated vision based tracking techniques for future hypersonic Earth re-entries.

## 2 Visual Servoing Architecture

In this section we introduce the equipment and setup for the re-entry. We also present the image Jacobian and the approximations applied to it for this particular application.

### 2.1 Equipment setup

The actuation unit is a Directed Perception PTU-47-17 high speed 2 axes pan and tilt unit. This unit hosts two identical 'Flea 2' black and white Point Grey cameras capable of running at 30Hz. The tracking camera with a 6mm lens and the spectrometer with a 25mm lens combined with a 300l/mm grating are mounted on the pan and tilt unit (PTU) payload bracket as shown in Figure 2. The spectrometer setup is briefly discussed in Section 6.3. A typical desktop CPU interfaces between the camera and PTU using an IEEE 1394b standard interface and serial communication respectively. Two additional hard drive disks were included in the host computer to save simultaneous streaming of images from both cameras. All vision processing and PTU movement tasks were handled by a C program written in Microsoft Visual Studio in a Windows based environment.

### 2.2 Image Jacobian

For an end effector mounted camera setup, tracking a target requires a known relationship between the change in target position on the image plane to the change in PTU pose. Using a pin hole camera model and a perspective geometric relationship between the target and the camera, an image Jacobian can be derived. Luca [Luca et al., 2008] and Corke [Corke, 1994] show a detailed derivation of this transformation. The resultant image Jacobian for a point  ${}^c\mathcal{O} = [x, y, z]$  expressed in the camera coordinates can be written as,

$$\dot{\mathbf{p}} = \mathbf{J} \times \dot{\mathbf{r}}$$

where  $\mathbf{J}$  is the interaction matrix,  $\dot{\mathbf{p}}$  is the image feature velocity on the image plane and  $\dot{\mathbf{r}}$  is the relative PTU velocity in Cartesian coordinates. This equation can be expressed as a matrix,

$$\begin{bmatrix} \dot{u} \\ \dot{v} \end{bmatrix} = \begin{bmatrix} \frac{f}{z} & 0 & \frac{-u}{z} & \frac{-uv}{f} & \frac{f^2 + u^2}{f} & -v \\ 0 & \frac{f}{z} & \frac{-v}{z} & \frac{-f^2 - v^2}{f} & \frac{uv}{f} & u \end{bmatrix} \begin{bmatrix} T_x \\ T_y \\ T_z \\ \omega_x \\ \omega_y \\ \omega_z \end{bmatrix}$$

where  $\dot{u}, \dot{v}$  are the velocities of the image feature with target coordinates on the image plane  $u$  and  $v$ .  $T_x, T_y, T_z$  and  $\omega_x, \omega_y, \omega_z$  are translational and rotational velocities of the end-effector with respect to the camera frame in a fixed camera system respectively.  $f$  is the focal length of the camera lens in pixels.

For a 2 DOF pure rotational motion in the pitch and yaw axes of the PTU the above matrix can be reduced to the following equations,

$$\dot{u} = \frac{f^2 + u^2}{f} \omega_y \quad \text{and} \quad \dot{v} = \frac{f^2 + v^2}{f} \omega_x$$

In forming the equations above, a few approximations need to be addressed. The off-axis mounting of the tracking camera leads to the introduction of the two offset terms  $X_o$  and  $Y_o$  when transforming the PTU coordinate system to the camera coordinates. The yawing and pitching motions about the  $y$  and  $x$  axes introduce PTU translation velocities in the  $x$ - $z$  and  $y$ - $z$  planes respectively. Assuming that the coordinates of the object being tracked are  ${}^c\mathcal{O} = [x, y, \infty]$  and the offset terms  $X_o, Y_o \approx 0$ , the translational motion induced can be approximated as zero.

## 3 Visual Feedback Control

In this section we present the model of the system that was used to implement both the visual feedback and dynamic feed-forward control strategies as shown in Figures 3 and 6 respectively. For simplicity, all system modelling and analysis will assume a single axis system. Target movement is assumed only about the  $y$ -axis that corresponds to the horizontal line on the  $u$ - $v$  image plane.

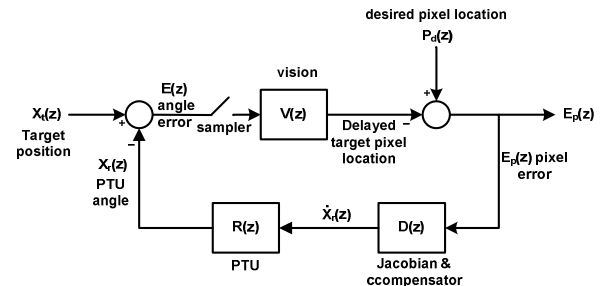


Fig. 3. Block diagram of the feedback control system

### 3.1 System modelling

The visual servoing system is a single rate system that runs at the video update rate of 30Hz. Each module of this system is represented as a function in discrete  $z$ -domain notation.

For a fixating task, the output of the model describes the image plane pixel error  $E_p(z)$ , for a given target motion  $X_t(z)$ . The desired pixel location  $P_d(z)$ , remains unchanged at the centre of the image plane with coordinates  $u_d$  and  $v_d$  depending on the resolution being used. This input drives the visual feedback loop where any change in target motion will result in a pixel error. The discrepancy between the PTU and the target position is obtained by querying the PTU controller, resulting in the error signal  $E(z)$ , in radians.

The compensator comprises of the Jacobian conversion and a proportional feedback gain  $K_p$ . This gain was selected using analytical and experimental techniques to provide a critically damped response.

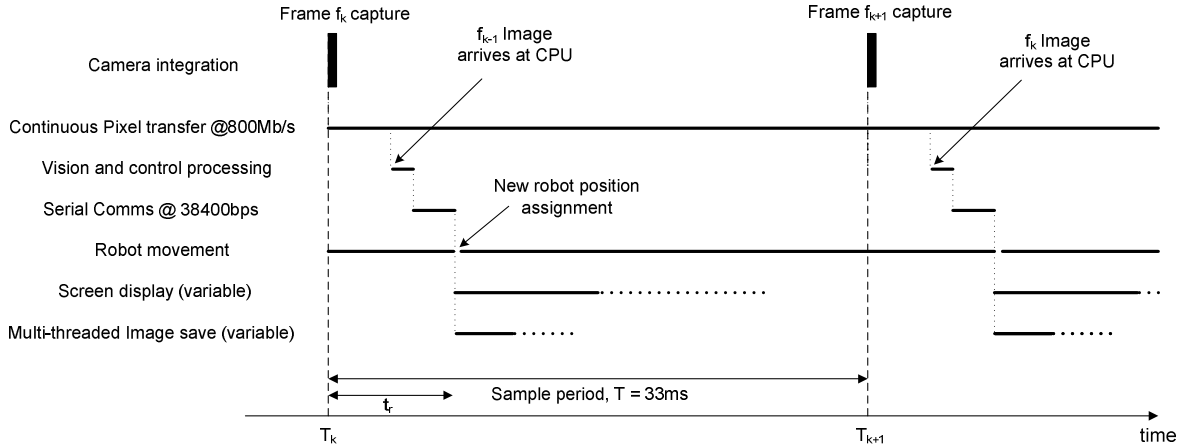


Fig. 4. System timing diagram for a single camera operation running at 640x480 pixel resolution. Note that in this case there is a large initial target movement where the PTU axes cannot achieve the commanded pose before the next shutter event. The PTU movement continues until re-commanded.

The vision system  $V(z)$ , is modelled as a delay for a single sample period  $K_{lens}/z$ , where  $K_{lens}$  is an approximation of the lens gain for a particular focal length set on the camera. For small angular target changes per sample period this gain can be approximated as the focal length of the lens in pixels/rad.

The PTU  $R(z)$ , is composed of a combination of three parts, the PTU dynamics  $R_d(z)$ , described in subsection 3.2, an integrator  $z/z-1$ , and a single frame delay  $1/z$ . The PTU operates in real time and starts to change pose as soon as a command reaches the controller. However, a delay is introduced since the change in PTU position is only sensed by the system at the next shutter event.

### 3.2 PTU dynamics

The PTU acceleration and velocity information is provided by the manufacturer and is programmable to user defined settings. The PTU velocity is divided into two segments: above and below a base velocity of 0.9rad/s. Due to hardware limitation, velocities above the base velocities  $V_b$  (achievable up to 3.6rad/s) take a measurable amount of time  $\Delta t_a$  and  $\Delta t_b$  to accelerate and decelerate to the requested velocity.

To simplify the analysis the PTU is only operated at base velocities resulting in an effective instantaneous acceleration and deceleration. In forming this assumption the moment of inertia is approximated as zero due to the insignificant weight and offset distance of the cameras from the centre of each axis. This simplified dynamic behaviour of the PTU can be modelled as a non-linear saturation function  $f(v)$ , where  $\dot{X}_r(z)$  is the input velocity command.

$$f(v) = \left\{ \begin{array}{ll} \dot{X}_r(z) & \text{if } -0.03 < v < 0.03 \\ 0.03 & \text{if } v \geq 0.03 \\ -0.03 & \text{if } v \leq -0.03 \end{array} \right\}$$

The above equation is graphically represented in Figure 5.

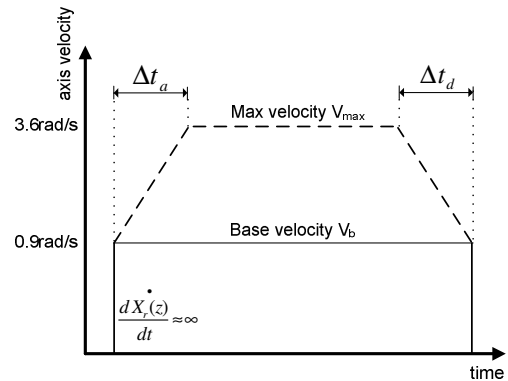


Fig. 5. Approximate velocity-time profile of the PTU for a large angular movement with negligible load characteristics and moment of inertia approximated as zero

### 3.3 System timing

Each component within the visual servoing loop contributes towards system latency. The behaviour and stability of this visual servoing system primarily depends on the image transfer time between the camera and the host computer. Figure 4 shows the approximate duty cycle of tasks over a sample period  $T$ .

The primary cause of latency in this system was found to be the pixel transfer which occurs between the camera and the host computer. The image processing algorithm and communication between the software and the PTU takes approximately 4ms which is relatively insignificant when compared to the delay caused by the transfer of pixels. The pixel transfer contributes approximately 30ms to 90ms of delay, depending on the size of the image and number of cameras on the fire-wire bus.

Image  $f_k$  only arrives at the CPU after the  $f_{k+1}$  camera shutter event has elapsed, i.e. the image that is processed to determine PTU angles uses target information out-dated by a single frame. This causes instability in the system and can be compensated by dampening the system dynamics. This is achieved by introducing a proportional gain  $K_p$  on the feedback path. Note that the latency was found to increase by up to three sample periods when the number of cameras on the same bus or single camera resolution was increased.

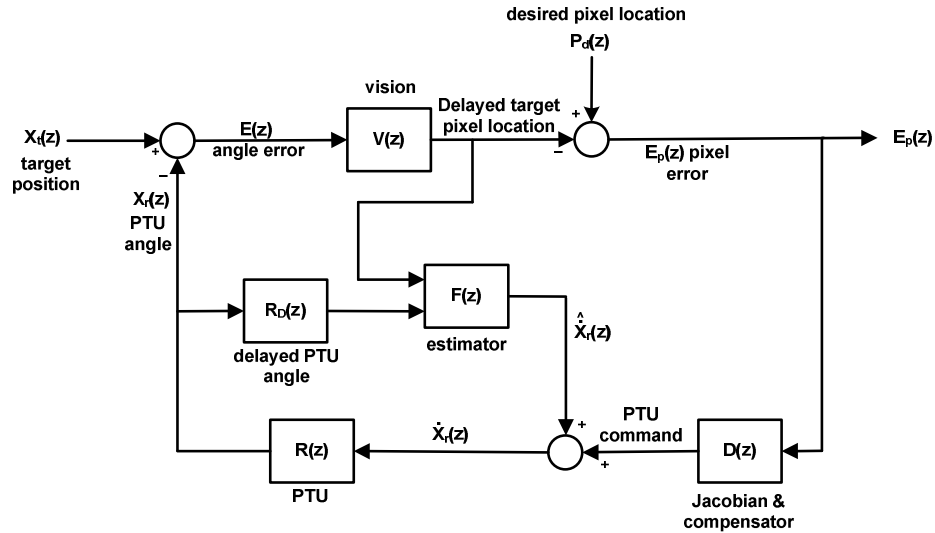


Fig. 6. Block diagram of the feed-forward control system.

## 4 Visual Feedforward Control

The feedback control discussed in the previous section was found to be sufficient to track the Hayabusa re-entry and obtain spectral images of the emissions using a 25mm lens that provided a  $9^\circ$  FOV. However, since the system capability can be increased without the need for any additional hardware, feed-forward is implemented and tested on tracking the ISS. This configuration could achieve a much higher tracking performance with the ability to maintain the target within a narrower FOV. Figure 6 shows a simplified feed-forward block diagram.

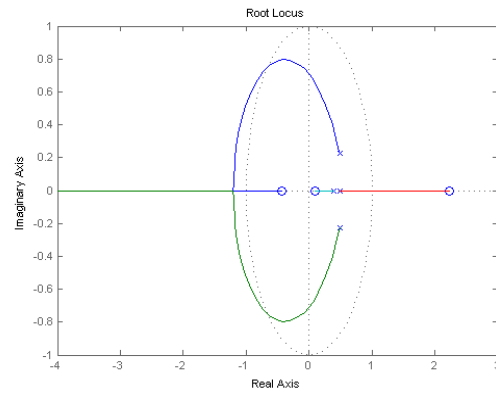
### 4.1 System modelling and analysis

The objective of implementing feed-forward control is to alter the dynamics of the system and increase stability. The primary cause of this instability in feedback control is the latency in the vision system discussed in Section 3.3. In a feedback system the dynamics are altered by the use of a proportional gain, but at the expense of tracking performance. To overcome this, an estimator  $F(z)$ , is used in the form of an alpha-beta filter. The filter uses the delayed PTU and target position information and provides an estimate of the current target velocity on the image plane. Two new terms are introduced in the model; a delayed PTU position,  $R_D(z)$  and the estimator  $F(z)$ .

The estimator is implemented in two steps: (a) The delayed target position is estimated and (b) the current velocity is predicted. The estimation involves the use of two quantities; the output of the vision system and the delayed PTU movement. Both are required to avoid ambiguity between the actual target movement sensed by the camera and the apparent movement of the target due to PTU motion. The term  $R_D(z)$  represents a single frame delay, *i.e.*  $R_D(z) = R(z) \cdot z^{-1}$ . The delay is introduced to align the measurements between vision and the PTU, as the latter operates in real time. To analyse the system stability, a closed loop transfer function was derived,

$$\frac{E_p(z)}{X_t(z)} = \frac{V(z)[1 - R(z)R_D(z)F(z)]}{1 + V(z)D_N(z)(D(z) + F(z))\left(\frac{R(z)}{1 - R(z)R_D(z)F(z)}\right)}$$

where  $D_N(z)$  is  $1/K_{lens}$ , the inverse Jacobian approximation assuming small angle changes per sample period.


 Fig. 7 Root locus plot with  $K_p$  0.3,  $\alpha$  0.8 and  $\beta$  0.3. Poles are marked with 'x' and zeros with 'o'.

It is clear from Figure 7 that the poles of the above transfer function are within the unit circle and are therefore asymptotically stable with proportional gain  $K_p$  of 0.3 and alpha-beta estimator gains set to 0.8 and 0.3 respectively.

## 5 Experiments

The system discussed in previous sections was tested on tracking a number of indoor and outdoor objects to assess the performance of both the control and vision algorithms. The vision and control testing was conducted independently with emphasis on tuning system parameters for optimum tracking.

Three categories of system tests are conducted in the following chronological order; test prior to the re-entry, Hayabusa re-entry tracking & ISS tracking.

### 5.1 Vision algorithm

A number of tests were conducted to assess the suitability of LK pyramidal approach for the re-entry tracking application. To undertake such a test, a close representation of the actual re-entry was created. The

parameters of the Hayabusa re-entry were expected to be similar to that of the Stardust re-entry [Winter et al, 2007] and thus pre-recorded observation videos of this re-entry were used to perform the analysis.

Figure 8 below shows the feature identification sequence using pre-recorded Stardust SRC re-entry video (a red dot 3 pixels in diameter is the feature the algorithm is attempting to track). Stardust initially appears as a point source object which makes it ideal to be identified and tracked using the LK scheme. This technique determines the velocity for an individual pixel and calculates the optical flow for subsequent frames. As the spacecraft gets closer, the projection on the 2D image plane is displayed as a patch of pixels, however, the LK algorithm coped as long as changes were small between frames and a sharp contrast was maintained between the night sky and the edge of the glowing heat shield.

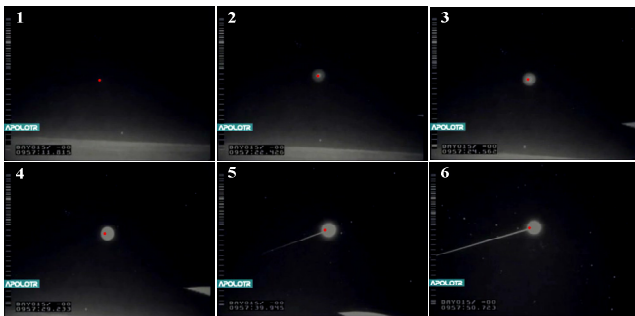


Fig. 8. Images are snapshots from the LK tracking test on the pre-recorded Stardust SRC re-entry video. The red dot overlaid on the image shows the feature it is tracking

### 5.2 Simulation and system tests

The first set of simulation and experiments tests are conducted prior to the re-entry on different target trajectories to establish; a) whether the model developed for this system was accurate and could be used as the basis for further development and b) to determine whether the system was capable of fixating on the estimated Hayabusa spacecraft velocity and record spectral data using the co-aligned spectrometer camera simultaneously throughout the re-entry event.

To verify whether the system complied with the above requirements, the simulation and the actual visual servoing rig were tested with targets exhibiting constant and sinusoidal velocities.

The relative constant velocity motion was set to 0.5rad/s with Figure 9 showing the tracking performance of the system in the y-axis (pan) which corresponds to the horizontal image plane axis. The solid and dashed lines show the actual system and the Simulink model respectively. Tracking steady state error of about 25 pixels can be seen for the constant velocity motion. Similar response for both the simulation and actual system performance is evident for a given target motion, validating the approximations made during the design phase.

For the sinusoidal motion, a simple pendulum was created by suspending an object from the ceiling. The pendulum motion of the target was set at an approximate maximum velocity of 0.5rad/s and peak amplitude of 0.25 radians (decaying over time). The system fixated on the target with a maximum error of 50 pixels peak-peak when running at a 640x480 pixel resolution.

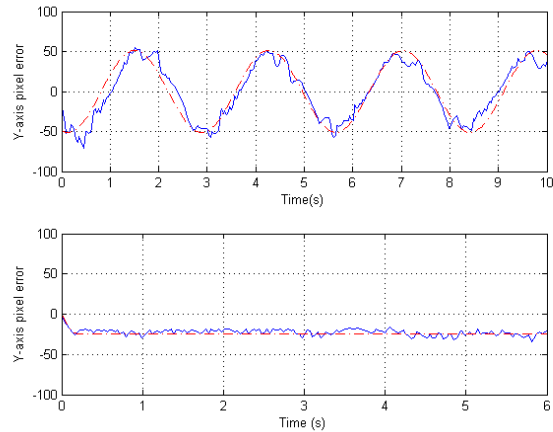


Fig. 9 Response of the pan (y-axis) of the system (solid) and model simulation (dashed) to different target trajectories. The plots show the y-axis pixel error response of the system for a constant velocity (bottom) and a sinusoidal (top) target trajectory at 640x480 pixel resolution.

The results in Figure 10 show the comparison between feedback and feed-forward control strategies for the same target trajectory characteristics. A significant increase in performance can be seen when using feed-forward compared to proportional feedback control. The constant velocity motion shows a steady state error of approximately 20 pixels for the feedback system due to the latency in the vision system while feed-forward fixates on the desired pixel location without any significant lag. Similar results were obtained for the sinusoidal target trajectory test with a peak to peak error of about 100 pixels for feedback while 20-25 pixels for feed-forward.

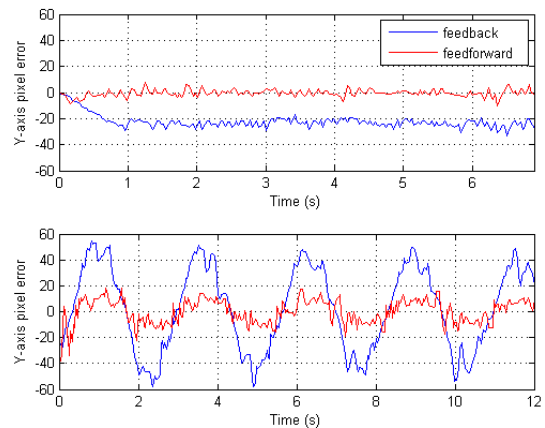


Fig. 10. Pan pixel error response of the system for a constant velocity (top) and a sinusoidal (bottom) target trajectory at 640x480 pixel resolution. The target is approximately 0.25 radians in amplitude and with a velocity of 0.5rad/s (max) and 0.5rad/s for the sinusoidal and constant velocity target trajectory respectively.

To validate the improvements using the feed-forward tracking strategy, a field experiment was set up to track the ISS. The same hardware used for tracking the re-entry was set up to track the ISS. For this test, the tracking camera was fitted with a 25mm lens which provided a higher magnification (9° FOV). The estimated velocity of ISS across the image plane for both test runs was approximately 300-350pixels/second (running at 600x800 pixels). The camera parameters were set to the same

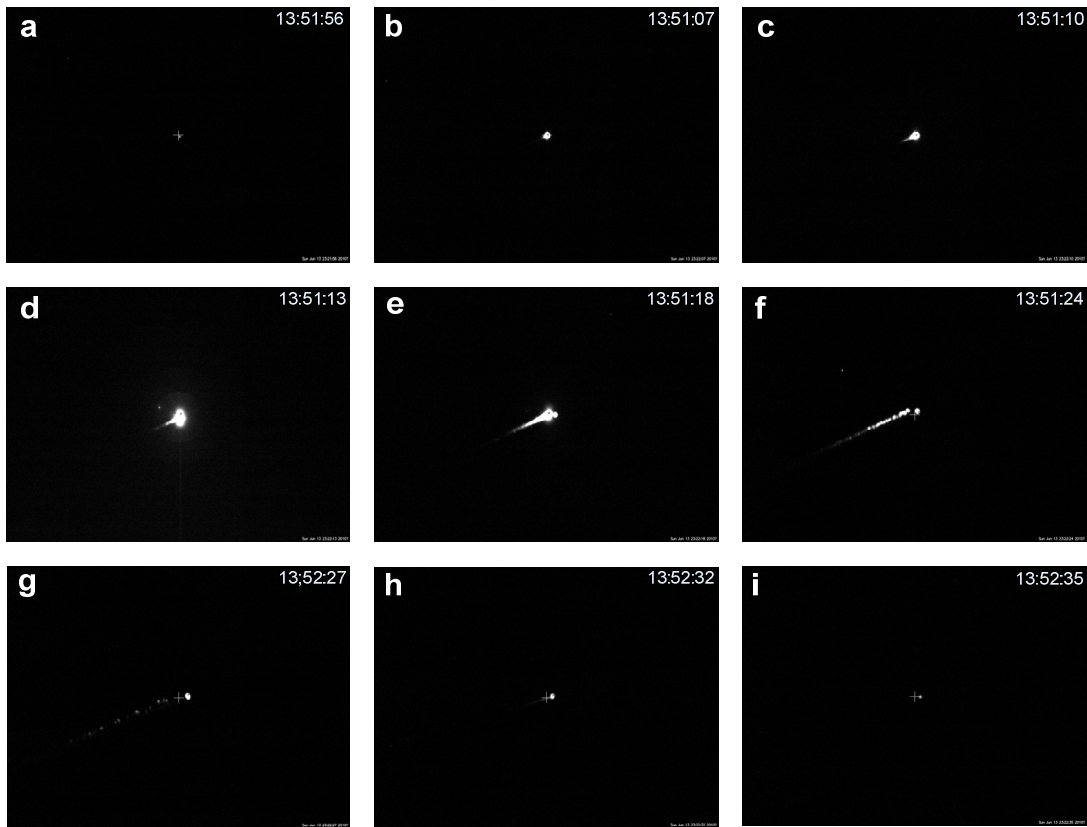


Fig. 11 Hayabusa spacecraft raw images captured during the re-entry from the tracking camera. The sequence of images are in increasing order of time from left to right and top to bottom with a variable interval of time between them. Note that the overlaid time on the top right is in UTC

configuration as for the Hayabusa re-entry tracking with the observation made under similar lighting conditions.

The apparent motion of the ISS across the sky from a ground based position was relatively slow; however, the effective motion across the image plane was comparable to that of the Hayabusa re-entry when observed through a narrow FOV lens. In addition, the velocity of ISS was not constant as viewed from a ground observation location. Since the depth information was lost in perspective photogrammetric, only the velocity perpendicular to the camera was accounted for resulting in a varied image plane velocity. However, since the change in velocity due to the serial nature of the test was small, the velocities were assumed the same (with slightly faster velocities experienced across the image plane for the feed-forward test).

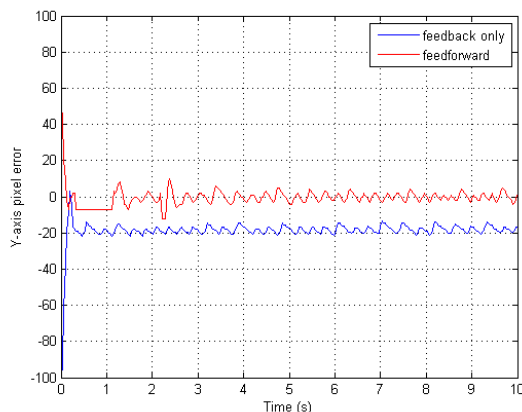


Fig. 12. Y-axis error response for ISS through a 25mm lens

The fixation performance of the feed-forward control scheme was better even after the fact that the feedback control experienced relatively slower target velocities on the image plane. The results in Figure 12 show an improvement of 20 pixels with feed-forward implemented when using a 25mm FOV lens on the tracking camera.

## 6 Hayabusa Tracking and Emissions Spectrum

This section outlines the performance of the visual feedback system implemented for tracking the Hayabusa SRC. In addition, a brief overview is included of the spectrometer equipment used, calibration and the results obtained from the re-entry spectroscopy.

### 6.1 Hayabusa tracking

The Hayabusa sample return capsule was tracked using a visual feedback system discussed in Section 3. The apparent relative velocity of the spacecraft on the image plane was variable throughout the re-entry. The initial visible approach of the spacecraft was towards the cameras setup and therefore a small velocity vector was observed on the image plane resulting in less than 10 pixels of error as observed in the first 300 samples on the pan axis error. As the perpendicular component of the velocity relative to the cameras increases, the image plane velocity vector increases, amplifying the error to around 20-30 pixels.

Similar behaviour can be seen in the tilt axis response. Note that since most of the capsule velocity is forward not much X-axis or tilt pixel error is observed.



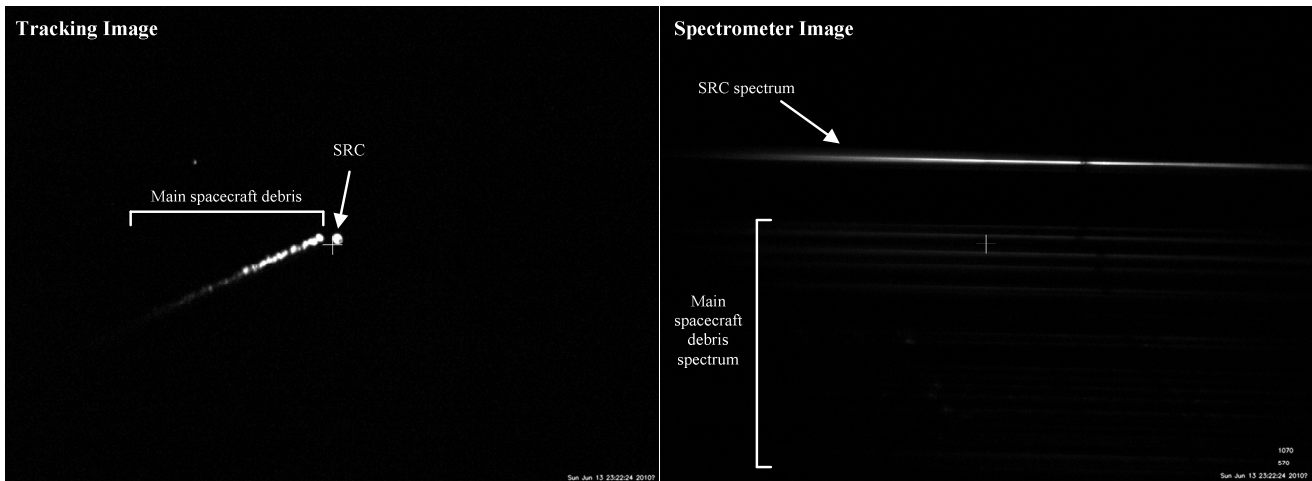


Fig 13. On the left is one of the tracking images with the capsule leading the disintegrating spacecraft debris. Image on the right shows the raw spectrum image of the capsule at the top with additional spectral lines of the debris below.

Figure 14 shows the tracking performance of the system during the 45 second visible portion of the re-entry. A mean error of approximately 15 pixels & 5 pixels and a maximum angle deviation of  $0.9^\circ$  and  $0.3^\circ$  in the pan and tilt axes respectively was observed.

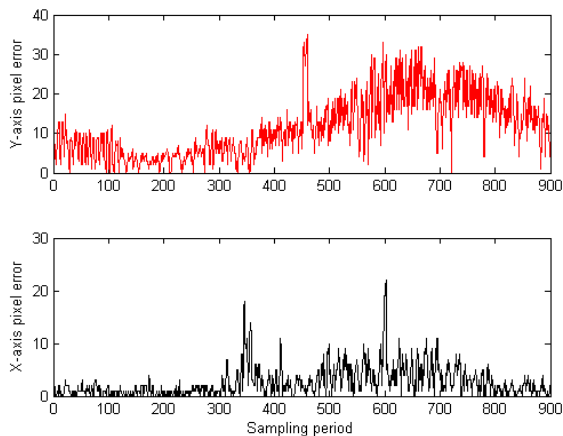


Fig. 14. Hayabusa sample return capsule tracking error profile for the period observed (operating at 1024x768 pixel)

Figure 11 shows the image recorded during the tracking of the Hayabusa spacecraft re-entry. The grey dot (3 pixels in diameter) overlaid on the SRC is the feature the control algorithm is attempting to centre.

## 6.2 Camera image mapping

The movement of the PTU in any axes causes the movement of both the tracking and spectrometer camera simultaneously. The fixed relationship between the cameras for any tracking task will induce an offset on the spectral and spatial axes of the spectrometer camera. Figure 13 (right) shows an image of the spectrum for the SRC on the top and several spectra below it on the lower half of the screen representing the main spacecraft debris.

Each object displayed on the tracking camera image can be mapped to a spectrum on the spectrometer camera image provided that the object is of sufficient intensity so that its spectrum can be detected. From Figure 13 (left), the SRC leads the debris and is seen close to the centre crosshair of the tracking camera image. The debris

field extends in two image plane axes; horizontally and vertically lagging from the centre of the image. The corresponding spectra of the SRC can be seen a third of the way from the top of the image with the individual spectrum of each spatially resolved section of the spacecraft debris displayed below it. Note that the lower spectra are skewed to the right. This is due to the fact that the observed debris appears to be displayed lower on the tracking camera. This offsets the wavelength scale for each of these spectra, which can be re-calibrated using the atmospheric absorption bands.

## 6.3 Spectrometer setup and calibration

The spectrometer setup uses a camera with a transmission grating, optimized for the near infrared (NIR) with a peak efficiency at 700nm, attached before the lens. The 300l/mm line spacing of the grating and its distance from the CCD allows a range of wavelengths from 450 to 900nm to be recorded on the CCD array with a resolution of 0.44nm/pixel. To obtain linear dispersion of the spectrometer and the response of the camera, the equipment was calibrated using a standard fluorescent lamp and an Optronic Laboratories OL200M standard source respectively.

The CCD sensor combined with a 25mm lens provides a  $9^\circ$  FOV with the resultant spatial resolution dependent on the distance of the target. The estimated slant range between the SRC and the optics varied around 60-100km which provided a resolution of 25-40 metres per pixel on the spectrometer respectively. Therefore, spatial information of the SRC could not be deduced.

## 6.4 Preliminary spectrum analysis

Of primary interest is the radiation emitted by the superheated shock layer formed in front of the spacecraft and in particular, the sample return capsule. Quantifying the radiation emitted by the shock layer provides an estimate of the total heat transfer to the skin of the spacecraft. This in turn may lead to a better understanding of the shock layer and aid in the design of more efficient thermal protection systems for future spacecraft.

An initial analysis of the spectrum for the sample return capsule from a single frame of data is shown in

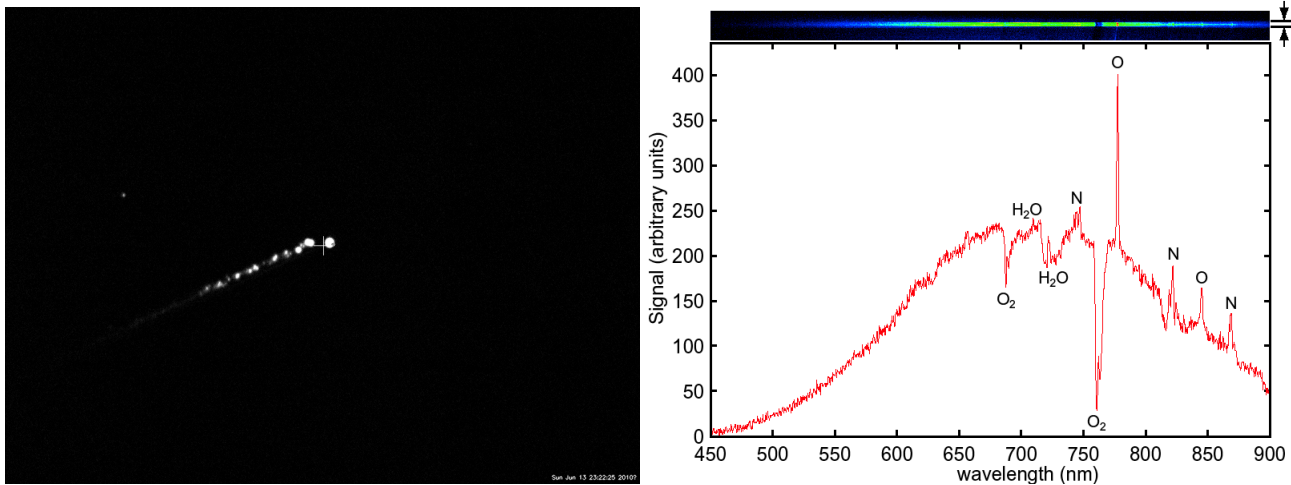


Fig. 15. On the left is one of the tracking images during the Hayabusa's reentry. Note that the target of interest is the re-entry capsule which is leading a trail of burning spacecraft. Image on the right shows the preliminary analysis of one of the spectral emission lines of the Hayabusa's re-entry capsule.

Figure 15 (right). The data is un-calibrated, so the Y-axis of the plot gives the raw response of the camera averaged across a strip of pixels 5x1024 shown on top right of Figure 15.

Several prominent spectral lines are present for atomic oxygen (777nm and 844nm) and atomic nitrogen (744nm, 821nm and 868nm). This is consistent with the molecular oxygen (O<sub>2</sub>) and nitrogen (N<sub>2</sub>) dissociating under extreme heat. There are also several prominent absorption features of H<sub>2</sub>O and O<sub>2</sub> due to atmospheric absorption. All other features are consistent with gas temperatures on the order of 4000-5000K. Further work is necessary to identify other emission and absorption features and to convert the raw output of the camera into a measurement of spectral irradiance.

## 7 Conclusion

This paper has presented an automated technique to track and record spectral emission for the atmospheric re-entry of Hayabusa. An improvement in the tracking scheme is also implemented post re-entry, using visual servoing feed-forward control. To prove the effectiveness various target trajectories are tested including the tracking of the ISS using a narrow FOV lens.

This paper ascertains that visual servoing techniques can provide improved tracking performance and higher resolution spectral images when observing re-entries of hypersonic space object. The tracking of the Hayabusa SRC and ISS using visual feedback and feed-forward control systems, respectively, have quantitatively shown the improvements in tracking performance which leads to better spatial resolution of the targets surface when utilizing optics in a co-aligned configuration. Given these results, future re-entry missions will be more inclined to accept the use of automation based optical instrumentation and incite further development in the field of visual servoing.

## 8 Acknowledgements

The authors would like to thank Richard Morgan (UQ) for suggesting the research program, Michael Jokic (USQ), Carolyn Jacobs (UQ) and Peter Jenniskens (SETI) for their efforts in organizing the Hayabusa ground

observation in collaboration with JAXA and NASA teams. Thanks also to Peter Corke (QUT) for his valuable comments on the preliminary versions of this paper.

## References

- [Bernardino et al., 1999] A.Bernardino and J.S.Victor. Binocular Tracking Integrating Perception and Control. *IEEE Trans. on Robotics and Automation*, vol. 15, no. 6, Dec 1999.
- [Bouguet, 1981] J.Y.Bouguet. Pyramidal Implementation of the Lucas Kanade Feature Tracker Description of Algorithm. Intel Corporation, Microprocessor Research Labs
- [Buttsworth et al. 2011] D.Buttsworth, P.Jacobs, D.Potter, N.Mudford, M.D'Souza, T.Eichmann, R.Morgan, P.Jenniskens, T.McIntyre, M.Jokic, C.Jacobs, B.Upcroft, R.Khan, H.Porat and A.Neely. Super-Orbital Re-entry in Australia – laboratory measurement, simulation and flight observation. *Proceeding in 28th International Symposium on Shock Waves*, 2011
- [Corke 1994] P.I.Corke. High Performance Visual Closed Loop Robot Control. PhD dissertation, University of Melbourne, Department of Mechanical and Manufacturing Engineering, July 1994
- [Corke et al., 1996] Peter I.Corke and Malcolm C.Good. Dynamic Effects in Visual Servoing Closed-Loop System. *IEEE transaction in Robotics and Automation*, vol 12, no.5, pages 671-683 October 1996
- [Eichmann et al. 2011] T.Eichmann, R.Khan, D.Buttsworth, and B.Upcroft. Radiometric Temperature Analysis of the Hayabusa Re-entry. 28th International Symposium on Shock Waves, 2011
- [Horvath et al., 2010] Thomas J.Horvath, Deborah M.Tomek, Karen T.Berger, Scott C.Splinter, Joseph N.Zalameda, Paul W.Krasa, Steve Tack, Richard J.Schwartz, DavidM.Gibson, and Alan Tietjen. The HYTHIRM Project: Flight Thermography of the Space Shuttle During Hypersonic Re-entry. *Proceedings in AIAA 2010-241*, 48<sup>th</sup> AIAA Aerospace Science Meeting Jan 4-7, Orlando, Florida, 2010
- [Hutchinson et al., 1996] Seth Hutchinson, Gregory D.Hager and, Peter I.Corke. A Tutorial on Visual Servo Control. *IEEE transactions on Robotics and*

- Automation*, vol. 12 no. 5, October 1996
- [Jenniskens et al., 2006] P.Jenniskens, P.F.Wercinski, J.Olejniczak, M.Wright, G.Raiche, D.Kontinos, P.N.Desai, R.E.Spalding, K.Sandquist, G.Rossano, R.W.Russell, D.O.Revelle, D.Hladiuk, and A.R.Hildebrand. Surface Heating from Remote Sensing of the Hypervelocity Entry of the NASA Genesis Sample Return Capsule. *44<sup>th</sup> AIAA Aerospace Sciences Meeting and Exhibit*, Reno, Nevada, 9-12 Jan 2006.
- [Jenniskens, 2008] P.Jenniskens. Observations of the STARDUST Sample Return Capsule Entry with a Slit-less Echelle Spectrograph. *46<sup>th</sup> AIAA Aerospace Sciences Meeting and Exhibit*, Reno, Nevada, 7-10 Jan 2008.
- [Khan 2012] R.Khan. Observation of the Hayabusa Spacecraft Re-entry: An Image-Based Visual Servoing Approach. MPhil dissertation, University of Queensland, Department of Mechanical and Mining Engineering, Dec 2012
- [Khan et al. 2010] R.Khan, T.Eichmann, B.Upcroft, and D.Buttsworth. Vision Based Tracking of HIFiRE Test Vehicle Re-entry. 10<sup>th</sup> Australian Space Science Conference, 2010. (ISBN 978-0-9775740-4-9)
- [Luca et al., 2008] Alessandro De Luca, Giuseppe Oriolo and Paolo Robuffo Giordano. Feature Depth Observation for Image-based Visual Servoing: Theory Experiments. *The International Journal of Robotics Research* 2008
- [Mcintyre et al. 2012] T.Mcintyre, R.Khan, R.Morgan, D.Buttsworth and B.Upcroft. Visible and Near Infrared Spectroscopy of Hayabusa Re-entry using semi-autonomous tracking. *Proceeding in 50th AIAA Aerospace Science Meeting*, 2012
- [Papanikolopoulos et al., 1993] N.P.Papanikolopoulos, P.K.Khosla, and T.Kanade. Visual tracking of a moving target by a camera mounted on a robot: A combination of vision and control. *IEEE transaction in Robotics and Automation*, vol 9, no.1, pages 14-35 1993
- [McHarg et al., 2008] M.G.McHarg, H.C. Stenbaek, and T.Kanmae. Observation of the STARDUST Sample Return Capsule Entry using a High Frame Rate Slit-less Spectrograph. *46<sup>th</sup> AIAA Aerospace Sciences Meeting and Exhibit*, AIAA 2008-1211, Reno, Nevada, 7-10 Jan 2008.
- [Song et al., 2009] W.Song, M.Minami. Stability/Precision Improvement of 6-DOF Visual Servoing by Motion Feedforward Compensation and Experimental Evaluation. *Proceedins in IEEE International Conference on Automation and Robotics*, Kobe, Japan, May 12-17 2009.
- [Tack et al., 2010] Steve Tack, Deborah M.Tomek, Thomas J.Horvath, Harry A.Verstynen, Edward J.Shea. Cast Glance Near Infrared Imaging Observation of the Space Shuttle During Hypersonic Re-entry. *Proceeding in AIAA 2010-243*, 48<sup>th</sup> AIAA Aerospace Science Meeting Jan 4-7, Orlando, Florida, 2010
- [Uesugi, 2003] K.T.Uesugi. Space Engineering Spacecraft (MUSES) Program in ISAS Featuring Its latest Mission HAYABUSA. *Proceedings in Intl. Conference on Recent Advances in Space Technologies*, 2003.
- [Winter et al, 2007] M.Winter and G.Herdrich. Spectroscopic Observations of the STARDUST Re-Entry in the Near UV. *39<sup>th</sup> AIAA Thermophysics Conference*, Miami, FL, AIAA 2007-4050, 25-28 Jun 2007.
- [Zalameda et al. 2010] Joseph N.Zalameda, Alan B.Tietjen, Thomas J. Horvath, Deborah M.Tomek, David M.Gibbs, Jeff C.Taylor, Steve Tack, Brett C.Bush, David Mercer, Edward J.Shea. Application of a Near Infrared Imaging System for Thermographic Imaging of the Space Shuttle during Hypersonic Re-entry. *Proceeding in AIAA 2010-245*, 48<sup>th</sup> AIAA Aerospace Science Meeting Jan 4-7, Orlando, Florida, 2010